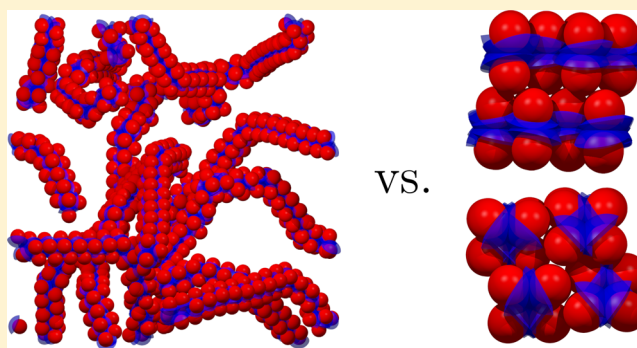


Phase Diagram of One-Patch Colloids Forming Tubes and Lamellae

Zdenek Preisler, Teun Vissers,* Frank Smallenburg, Gianmarco Munaò, and Francesco Sciortino

Dipartimento di Fisica, Università di Roma "Sapienza", Piazzale Aldo Moro 5, 00185 Roma, Italy

ABSTRACT: We numerically calculate the equilibrium phase diagram of one-patch particles with 30% patch coverage. It has been previously shown that in the fluid phase these particles organize into extremely long tubelike aggregates (G. Munaò et al. *Soft Matter* 2013, 9, 2652). Here, we demonstrate by means of free-energy calculations that such a disordered tube phase, despite forming spontaneously from the fluid phase below a density-dependent temperature, is always metastable against a lamellar crystal. We also show that a crystal of infinitely long packed tubes is thermodynamically stable, but only at high pressure. The full phase diagram of the model, beside the fluid phase, displays four different stable crystals. A gas–liquid critical point, and hence a liquid phase, is not detected.



INTRODUCTION

Because of recent progress in soft matter physics and chemistry, a wide variety of colloidal particles is now available. These colloids can be used as simple model systems to investigate the formation of complex supracolloidal structures, starting from isolated particles with methods analogous to those used in supramolecular chemistry.^{1–3} In this context, bottom-up approaches, where new materials are created via self-assembly of particles with nonisotropic interaction patterns,^{4–7} are a topic of considerable interest. A special subclass of these particles is constituted by the so-called “patchy” colloids, particles with a certain number of spots on their surface where they can form directional bonds.^{8–10} It has been shown that tuning the size and shape of the patches can lead to a rich variety of self-assembled clusters, such as micelles, helices, or disks,^{11–15} in addition to various crystalline structures and other ordered phases.

Simulations and theoretical studies have provided accurate results describing phase equilibria of colloids with a single patch^{16–19} as well as for multiple patches in a variety of geometries.^{10,20–23}

An elementary example of patchy particles are Janus colloids^{11,24–28} with a single attractive patch that covers one-half of the surface. These colloids have attracted a significant amount of interest because of both their potential technological applications and their peculiar self-assembly properties.^{29,30} However, experimental investigation of the cluster formation and characterization of the self-assembled structures is not always straightforward, especially because thermodynamically stable structures may compete with structures that are kinetically favored, preventing the observation of true equilibrium states.

In a previous work,³¹ we systematically investigated a simple model of one-patch particles interacting via a Kern–Frenkel potential³² for values of the patch surface coverage χ ranging

from small patches to Janus particles.^{33–35} Here, χ is defined as the ratio between the attractive patch and the total surface area of the particle. We unexpectedly found that for a specific value of the patch coverage, $\chi = 0.3$, long and persistent tubelike aggregates spontaneously appear at sufficiently low temperatures. The formation of such tubes, or wires, is rather sharp, and small changes in density and/or temperature induce significant variations in the average tube size. The formation of similar structures is commonly observed in the self-assembly of biological systems.^{36–38} Additionally, experimental studies of a large variety of surfactant molecules have shown the formation of wormlike^{39,40} and other elongated micelles, including tubes, ribbons, and cylinders.^{41,42} The structure of these micelles leads to viscoelastic properties which are useful for a range of applications.⁴⁰ While the shape and size of these surfactants may vary, their interactions in a solvent are characterized by effective attractions between the solvophobic part of each molecule, analogous to the attractive patch on a Janus particle. In fact, it was recently reported that Janus particles with a soft potential can form wormlike micellar structures as well.⁴³

In this work we perform a detailed analysis via Monte Carlo (MC) simulations of the single-patch Kern–Frenkel model with coverage $\chi = 0.3$ to determine if the *spontaneous* formation of tubelike structures is an intermediate step on the way to a thermodynamically stable crystal phase consisting of tubes. In other words, we investigate if a low-density phase composed of randomly oriented tubes is thermodynamically stable or if such a phase is kinetically trapped in a metastable state with respect to a crystal structure.

To properly investigate the stability of this peculiar phase, we present a complete equilibrium phase diagram by means of

Received: April 24, 2013

Revised: June 19, 2013

Published: July 31, 2013

free-energy calculations and thermodynamic integration methods, including both ordered and disordered phases. The evaluation of the phase diagram for particles with directional interactions requires as a first step a nontrivial search of all candidate crystal structures that must be tested for stability. We implement a wealth of different techniques to characterize them. To do this, we employ the so-called “floppy box” method,⁴⁴ which allows us to generate a wide set of possible crystals. In addition, we explore the self-assembly of crystal nuclei from the fluid and spontaneous solid–solid transitions. The paper is organized as follows: in the next section we describe the model, technical details, and simulation strategies. Then we proceed with stable crystal structures and their properties and discuss the behavior of the disordered phases. Finally, we discuss the equilibrium phase diagram and present our conclusions.

MODEL AND SIMULATION DETAILS

To describe the patchy-particle interactions, we employ the widely used Kern–Frenkel potential,

$$u^{\text{KF}}(\mathbf{r}_{ij}, \hat{\mathbf{n}}_i, \hat{\mathbf{n}}_j) = u^{\text{SW}}(r_{ij}) \Omega(\mathbf{r}_{ij}, \hat{\mathbf{n}}_i, \hat{\mathbf{n}}_j) + u^{\text{HS}}(r_{ij}) \quad (1)$$

where $u^{\text{SW}}(r_{ij})$ is a square well interaction potential

$$u^{\text{SW}}(r_{ij}) = \begin{cases} -\epsilon & \text{if } \sigma < r_{ij} \leq \sigma + \Delta \\ 0 & \text{if } r_{ij} > \sigma + \Delta \end{cases} \quad (2)$$

where ϵ is the well depth, r_{ij} the distance between particle i and j , σ the particle diameter, Δ the interaction range, and $\Omega(\mathbf{r}_{ij}, \hat{\mathbf{n}}_i, \hat{\mathbf{n}}_j)$ a function depending on the orientations of two interacting particles.

$$\Omega(\mathbf{r}_{ij}, \hat{\mathbf{n}}_i, \hat{\mathbf{n}}_j) = \begin{cases} 1 & \text{if } \begin{cases} \hat{\mathbf{r}}_{ij} \cdot \hat{\mathbf{n}}_i > \cos \theta \text{ and} \\ \hat{\mathbf{r}}_{ji} \cdot \hat{\mathbf{n}}_j > \cos \theta \end{cases} \\ 0 & \text{otherwise} \end{cases} \quad (3)$$

Here \mathbf{r}_{ij} is a vector between particles i and j and $\hat{\mathbf{n}}_i$ and $\hat{\mathbf{n}}_j$ denote the orientation of particle i and j , respectively. The interaction range is set to $\Delta = 0.5\sigma$, and patch coverage fraction $\chi = 0.3$ (corresponding to a patch opening angle $\cos \theta = 0.4$). Finally, the choice of the hard-sphere potential u^{HS} guarantees that the particles do not overlap:

$$u^{\text{HS}}(r_{ij}) = \begin{cases} \infty & \text{if } r_{ij} \leq \sigma \\ 0 & \text{otherwise} \end{cases} \quad (4)$$

Two particles are bonded if the shortest distance between their surfaces is smaller than Δ and the vector joining their centers of mass intersects the attractive patch on both surfaces (see eqs 2 and 3). One can imagine the patch bonding volume as the intersection volume of a sphere with a diameter $\sigma + \Delta$ and a cone with an apex originating from the center of the sphere and an opening angle θ , as depicted in Figure 1.

In the following, we implement isobaric–isothermal (NpT) simulations in a cubic box to calculate the fluid equations of state. For the crystals, we implement an isotension–isothermal ensemble, i.e., the lengths of the simulation box lattice vectors and the angles between them are allowed to fluctuate independently. In all calculations, the maximum step sizes for translational, rotational, and volume moves are optimized such that 50% of the attempted MC moves are accepted. In addition

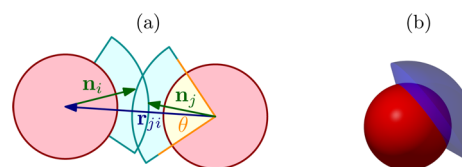


Figure 1. (a) Schematic representation of the patchy particles and their interactions; (b) a single patchy particle (red) with depicted Kern–Frenkel bonding volume (blue) for $\cos(\theta) = 0.4$ (corresponding to a patch coverage fraction $\chi = 0.3$ and range $\Delta = 0.5\sigma$).

to standard translational, rotational, and volume MC moves, aggregation volume bias (AVB) moves^{45,46} are implemented and used in case of disordered phase simulations. The length of the simulation runs is on the order of 10^6 – 10^7 MC cycles. In each MC cycle, N translational moves, N rotational moves, and one volume move are carried out, where N is the number of particles.

Technical Details Regarding the Calculation of the Phase Diagram. We calculated the equilibrium phase diagram of this model using free-energy calculations. The numerical methods used to calculate the chemical potential μ of all crystal phases are briefly summarized in the Appendix. After identifying the candidate phases, we use thermodynamic integration to locate coexistence points, i.e., points for which $\mu_{\text{I}}(p_{\text{coex}}, T_{\text{coex}}) = \mu_{\text{II}}(p_{\text{coex}}, T_{\text{coex}})$, where the two coexisting phases are labeled I and II. After determining a coexistence point between two phases, we draw a coexistence line by integrating the Clausius–Clapeyron equation⁴⁷

$$\frac{dp}{dT} = \frac{s_{\text{II}} - s_{\text{I}}}{v_{\text{II}} - v_{\text{I}}} = \frac{h_{\text{II}} - h_{\text{I}}}{T(v_{\text{II}} - v_{\text{I}})} \quad (5)$$

where s is the entropy per particle, h the enthalpy per particle, and v the volume per particle.

In our specific case, we calculate the chemical potential along the isotherms for $k_{\text{B}}T/\epsilon = 0.05, 0.14, 0.30$, and 0.50 and isobars $p\sigma^3/\epsilon = 3$ and 5 , where k_{B} is the Boltzmann constant.

The integration of the Clausius–Clapeyron equation is performed using smaller systems for the crystals, consisting of $N = 448$ and 600 . For the fluid we used $N = 1024$.

CRYSTAL STRUCTURES

Finding possible crystal structures is usually a difficult, tedious, and time-consuming job. Constructing crystal structures by hand, i.e., using an educated guess, is often feasible only in the case of some of the n -patch models in which the position and geometry of the patches are strongly correlated with the crystal structure symmetry.^{48,49} However, for one-patch models the stable crystal structures can become cumbersome to predict because more bonds per patch can be formed and the stability of crystals heavily depends on the patch width and range.

For this reason, we rely on a more systematic approach to search for crystal structures. We take advantage of the floppy box method which allows us to efficiently generate a wide set of possible crystals.^{35,44,50,51} This method is based on MC simulations of a small number of particles using a box with variable shape and volume in order to capture crystal unit cells. In this case, we explored unit cells of $N \in (3, \dots, 8)$ at multiple state points $k_{\text{B}}T/\epsilon \in (0.1, 0.145, 0.15)$, $p\sigma^3/\epsilon \in (0.1, 0.3, \dots, 3.7)$, resulting in three stable structures. For systems with a larger number of particles, this method becomes less efficient, making crystals with large unit cells more difficult to find.

Therefore, we also explore the formation of crystal structures starting from both the fluid phase and from solid initial states.³⁵ For example, we identified a fourth crystal structure (labeled **hcp**) by putting the particles on an hcp lattice and allowing them only to rotate. The same operation starting from an fcc lattice resulted in a metastable crystal.

Despite the simple particle design, we found four different stable crystals for this model (Figure 2), which we label **t-plane**,

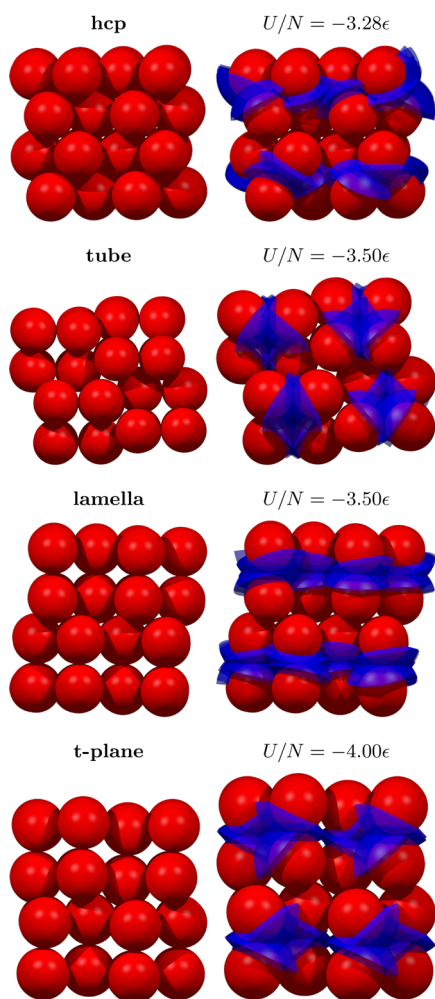


Figure 2. Stable crystal structures **hcp**, **tube**, **lamella**, and **t-plane**. Crystal structures are shown without (left column) and with (right column) bonding volume. The energy per particle in the crystal structure is given by U/N .

lamella, **tube**, and **hcp**. The **t-plane** and **lamella** structures have the same underlying lattice but have different bond orientations. The **tube** phase consists of infinitely long tubes packed in an ordered crystalline structure. We note that these tubes themselves have the same structures as those spontaneously formed from the fluid in the simulations (Figure 3). In the **hcp** crystal, the particles are on an hcp lattice with a disordered bonding pattern at higher temperatures yet pointing in a lamellar-like fashion at lower temperatures. The energetically most stable crystal is the **t-plane** in which each particle is bonded to eight neighbors, resulting in four bonds per particle, i.e., an energy per particle equal to $U/N = -4\epsilon$. This structure is essentially composed of interacting tubes, in which a small deformation of the tube structure allows for intertube

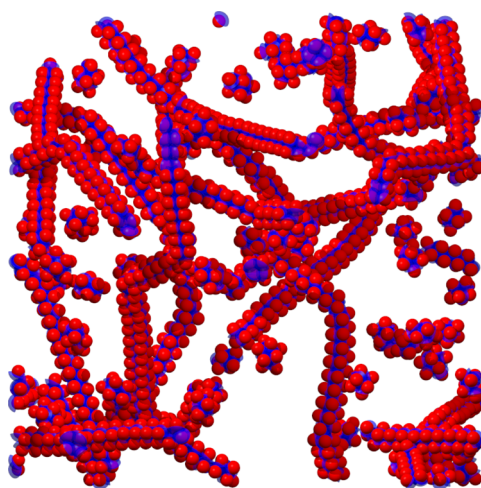


Figure 3. Typical simulation snapshot of a spontaneously created disordered tube structure. Here $N = 2000$, $k_B T/\epsilon = 0.13$, and $\rho\sigma^3 = 0.05$ after 10^8 MC cycles. This phase is metastable against a coexistence of a dilute fluid and lamellar crystals.

additional bonding. The crystals **tube** and **lamella** both have 3.5 bonds per particle, whereas **tube** has a higher maximum packing fraction. The **hcp** has the closest maximum packing fraction of all the crystals here, and it can have a maximum number of bonds per particle of ~ 3.28 .

■ CLUSTERS, FINITE TUBES, AND LAMELLAE

Tube Free Energy. In previous constant NVT MC calculations³¹ we observed the spontaneous formation of disordered tubelike structures at low temperatures and low densities. A snapshot of the system in the disordered tube phase is reported in Figure 3. This finding raised the question of whether these tubes are only a kinetically trapped state or a thermodynamically stable phase. At low T , the low-density fluid of Janus particles consists of a mixture of clusters of different sizes. The relatively low T and the slow growth kinetics associated with the growth of these clusters into tubes make it numerically hard to reach an equilibrium state in constant NVT simulations. To overcome this problem we resort to the evaluation of the free energy by calculating the cluster size distribution.^{35,52,53} Specifically, we implement the accurate methodology discussed in refs 35 and 52 that does not require the investigation of a bulk system but only the evaluation of the partition function of clusters of different size.

The underlying assumption of the cluster method is that the free energy and equation of state can be evaluated under the approximation of an ideal (or weakly interacting) gas of clusters with a cluster size distribution determined from single-cluster simulations.^{35,53} Specifically, the free energy of the cluster gas is approximated by that of an ideal gas of clusters plus a hard sphere excluded volume contribution:

$$\beta F(N, V, T) = \sum_{n=1}^{\infty} N_n \left[\ln N_n - 1 - \ln \mathcal{Z}_n + \frac{4\eta - 3\eta^2}{(1 - \eta)^2} \right] \quad (6)$$

where $\beta = 1/k_B T$, $\eta = \pi\rho\sigma^3/6$ is the packing fraction, N_n the number of clusters of size n , and \mathcal{Z}_n the partition function of a cluster of size n , given by

$$\mathcal{Z}_n = \frac{1}{(4\pi)^n \Lambda^{3n} n!} \int_V d\mathbf{r}^n \int d\Omega^n \exp[-\beta U(\mathbf{r}^n, \Omega^n)] c(\mathbf{r}^n, \Omega^n) \quad (7)$$

Here, \mathbf{r}^n and Ω^n denote the positions and orientations of the particles, respectively. Λ^3 is the thermal volume of a single particle. $c(\mathbf{r}^n, \Omega^n)$ is a constraint function that equals 1 if the n particles form a single continuous cluster and is 0 otherwise. The partition functions for each cluster size are calculated using single-cluster grand canonical MC simulations, as described in ref 35. Once all \mathcal{Z}_n values are known, it is straightforward to calculate the pressure and chemical potential at any density from the free energy.³⁵

In the single-cluster simulations, large clusters ($n \gtrsim 24$) at low temperature ($k_B T/\epsilon \lesssim 0.145$) are typically tube-shaped and identical to those shown in Figure 3. For these tubes, there is a clear preference for clusters with an even number of particles. However, the free-energy cost of adding two extra particles to a tube is essentially independent of n (i.e., $\mathcal{Z}_{n+2}/\mathcal{Z}_n$ is constant). As equilibrating large clusters is significantly slower than equilibrating small clusters, we performed single-cluster simulations up to cluster size $n = 60$ and extrapolated the values of \mathcal{Z}_n (for both odd and even n) to larger values. Interestingly, for smaller n values, cluster sizes that are a multiple of 8 are preferred: 8 particles can form a large number of bonds (typically 2.875 per particle, though 3 is possible). Non-tube-shaped clusters of size $n = 16$ and 24 typically consist of subclusters of size 8 that are chained together. A cluster consisting of 8 particles is depicted in Figure 4.

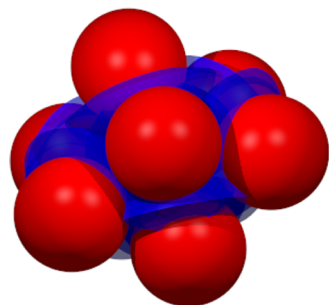


Figure 4. Snapshot of a cluster composed of eight particles generated by the technique described in the text at temperature $k_B T/\epsilon = 0.135$. A cluster is defined as a set of interconnected bonded particles.

In Figure 5, we show the predicted cluster size distributions $\rho_n \equiv N_n/V$ for different temperatures at one fixed ρ . The cluster size distribution is weakly T -dependent down to $k_B T/\epsilon = 0.140$, with clusters mostly composed by the 8-particle structure (with peaks at $n = 8, 16$, and 24). For lower T , most of the particles become incorporated in long tube structures. The density dependence of the average cluster size, shown in Figure 6 for six different temperatures, confirms the presence of a two-step self-assembly process on increasing density. First, particles organize in clusters with a typical size of 8. When density increases further, the number of particles in the cluster increases quite sharply once tubes become the thermodynamically relevant structures in this calculation.

Floating Lamellae. We will show later that the stable phase at low pressure is the lamella structure. The stability of the lamella crystal suggests that free-floating lamellae should also be able to form at low densities, similar to the observed

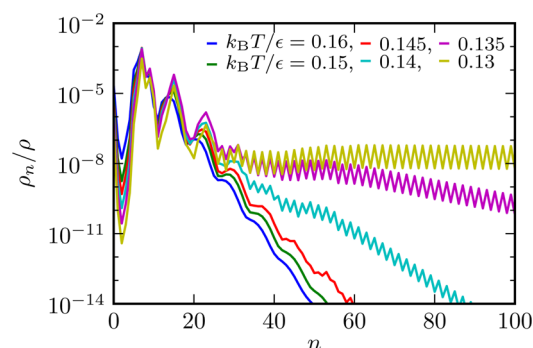


Figure 5. Cluster size distributions ρ_n/ρ at density $\rho\sigma^3 = 0.01$ as a function of cluster size n for six different temperatures ($k_B T/\epsilon = 0.16, 0.15, 0.145, 0.14, 0.135$, and 0.13). Note that the tubes (dominant for $k_B T/\epsilon \lesssim 0.14$) have a preference for even cluster sizes, while the smaller clusters prefer cluster sizes that are (approximately) multiples of 8. Here, ρ_n is the number density of clusters of size n .

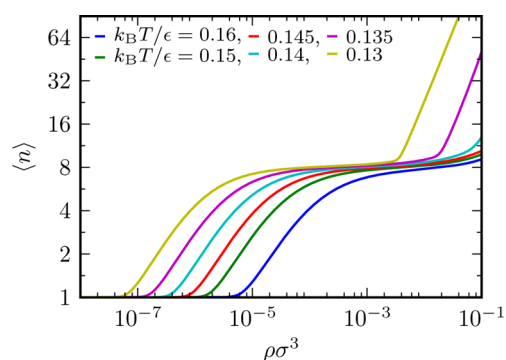


Figure 6. Average cluster size $\langle n \rangle$ as a function of the density ρ for $k_B T/\epsilon = 0.16, 0.15, 0.145, 0.14, 0.135$, and 0.13 .

formation of tubes. However, we have never observed the spontaneous formation of such structures in our lengthy MC simulations, suggesting that the growth of (metastable) tubes inhibits the formation of these sheetlike structures. To better understand this aspect, we performed MC simulations starting from an initial configuration containing a number of free-floating lamellae at low density and observed the evolution of these structures during the simulation. Depending on the density and temperature, some particles contained in the lamellae melt at the beginning of the simulation, creating a coexisting gas. After this coexisting gas is created, the system enters a kinetically trapped state where the floating lamellae are in coexistence with the gas (Figure 7). In this state we observed neither growth nor melting of the bilayers within our simulation time window (Figure 8).

We note that while an infinite lamella has an energy comparable to that of an infinite tube, the finite-sized lamellae have an energy higher than that of finite-sized tubes composed of the same number of particles. This explains why tubes spontaneously form in the fluid despite the fact that the infinite-sized lamellae are more stable.

■ PHASE DIAGRAM

The complete equilibrium phase diagrams in the T - p and ρ - T representations are shown in Figure 9 and Figure 10. In the T - p representation, appropriate for constant pressure experiments, the stable phase at the selected T and p is indicated and lines mark the transition from one phase to the next. The ρ - T

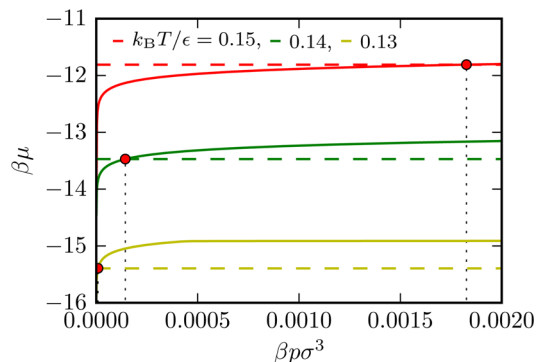


Figure 7. Chemical potential curves as a function of pressure for the lamella crystal (dashed line) and the dilute gas obtained from cluster distribution calculations (solid line) for $k_B T/\epsilon = 0.15, 0.14,$ and 0.13 . The corresponding coexistence pressures, at the points where these curves cross, indicated by red circles, are located at $\beta p \sigma^3 = 1.83 \times 10^{-3}, 1.43 \times 10^{-4},$ and 8.41×10^{-6} . The corresponding coexistence cluster gas densities are $\rho \sigma^3 = 1.47 \times 10^{-2}, 1.15 \times 10^{-3},$ and 6.67×10^{-5} . Note that the coexistence densities of the lamella phase are all lower than $\rho \sigma^3 = 1.05$.

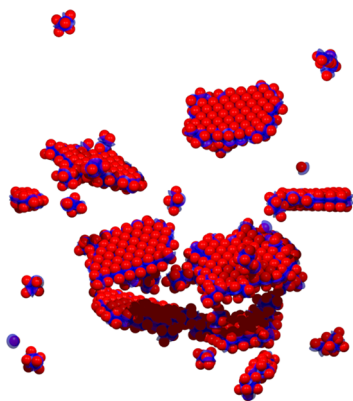


Figure 8. Snapshot of a disordered structure created starting from an initial configuration containing floating lamellae with $N = 1024, k_B T/\epsilon = 0.145,$ and $\rho \sigma^3 = 0.038$ after 10^6 MC cycles.

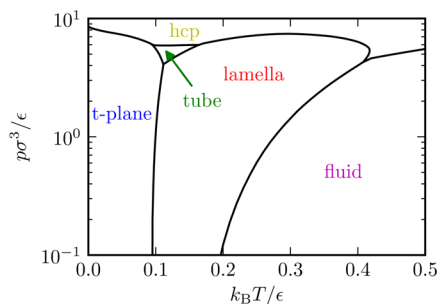


Figure 9. Calculated phase diagram in the T - p plane. Images of the different crystal structures **hcp**, **tube**, **lamella**, and **t-plane** are given in Figure 2.

representation, more appropriate for constant volume experiments, also conveys the information about the density region where the system phase-separates into two coexisting phases. For technical details about the calculations, see Model and Simulation Details and ref 35. At high pressure, the dense hcp phase is the most stable crystal for all temperatures. At lower T , the energetically most favorable structure is **t-plane**. As T is increased, this crystal converts to the **lamella** and then melts

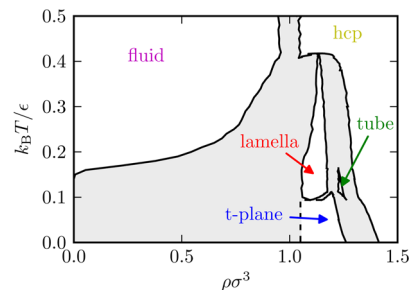


Figure 10. Phase diagram in the ρ - T plane. The dashed line indicates an upper bound for the **t-plane**-gas coexistence density. Below this density, we expect a mixture of the two phases.³⁵ The gray area indicates phase coexistence regions. The black lines that embed the gray area on both sides mark the coexistence densities of the coexisting phases.

into the fluid. At intermediate pressures, the **tube** crystal phase appears in a limited temperature interval.

In the ρ - T representation (Figure 10), we can see that at low densities the fluid phase is stable. To reach equilibrium upon decreasing T , the system phase-separates into a low-density fluid coexisting with a crystal phase. At high densities, where only crystals are present, we see that the most densely packed phase is **hcp**, which represents the hard sphere close packing. Furthermore, we observe that the **tube** crystal phase is more closely packed than the **lamella** and **t-plane** crystal phases, which allows it to be stable at intermediate pressures because the energies of the corresponding crystals are comparable.

Most of the coexistence points are located at rather high pressures, which helps to suppress the finite-size effects associated with the translational freedom of the individual bilayers or tubes.³⁵ To further suppress finite-size effects, we used large systems to calculate the coexistence points, i.e., $N = 3584$ particles for crystals **hcp**, **t-plane**, and **tube**, $N = 4800$ particles in the case of crystal **lamella**, and $N = 1024$ particles for the fluid. Although the tube phase occurs on only a small region of the phase diagram, we see that the crystal tube is more stable than other phases with a chemical potential difference of up to $\beta \Delta \mu = 0.1$, significantly more than our estimated error bars.

At low pressures, however, we are unable to determine exactly the coexistence densities. Nevertheless, the calculated chemical potentials are not influenced by this uncertainty because the pV contribution becomes very small as $p \sigma^3/\epsilon \rightarrow 0$. As mentioned in ref 35, the fact that individual lamellae are not connected via bonds suggests that the gas and **lamella** phase can mix freely in the coexistence region.

From Figure 7, we can read the densities of the fluid coexisting with the crystal phases. Note that the densities of the coexisting fluid at low temperatures are very low. For these low coexistence densities, we find from Figure 6 that the average cluster size is always lower than 24, which is the cluster size where randomly oriented tubes start to form spontaneously. Hence, a system at a total density between the coexistence densities (black lines embedding the gray area) will under equilibrium conditions always phase-separate in two phases, one being a crystal and the other one being the low-density fluid without tubes. Therefore, the disordered tube phase is metastable with respect to the coexistence between the low-density fluid and a crystal phase.

CONCLUSIONS

We have calculated the complete equilibrium phase diagram of Janus-like colloids with a patch coverage fraction of 30% and an interaction range equal to the particle radius by means of free-energy calculations and thermodynamic integrations. Several techniques were used to find various crystal structures. We used the floppy box method to generate a wide range of possible crystal candidates and have identified in total four different stable crystals. It should be noted that the existence of structures more stable than those investigated here can never be fully ruled out. For example, crystals with large unit cells can be difficult to find using the floppy box method and may not appear spontaneously in simulations.

As for the disordered structures observed, we have also employed the cluster size distributions to describe and characterize these structures. From free-energy calculations we have found that although tubes form spontaneously in constant *NVT* simulations at low density and temperature they are metastable with respect to a coexistence of a dilute fluid and a lamellar crystal. In addition, our results show that the spontaneous growth of tubelike structures from the fluid phase is preferred to the spontaneous creation of a lamella phase, which is stable at low pressures. However, a crystal phase (**tube**) containing tubes percolating on a lattice is thermodynamically stable upon compression in a small region of the phase diagram. This crystal phase is reminiscent of the ordered phases occurring in surfactant solutions that form wormlike micelles.³⁹

No gas–liquid phase transition has been found for this system; it is likely that this transition is suppressed by the formation of clusters, as has been observed in similar systems.^{31,35} In particular, the absence of this transition is due to the sudden formation of tubes. In contrast to what is observed for the pure Janus case ($\chi = 50\%$) in which a micellar gas phase coexisting with a liquid phase gives rise to an (anomalous) coexistence curve,³⁴ the appearance of long and persistent tubes (i.e., of structures that prevent a three-dimensional cluster percolation⁵⁴) suppresses this transition in the system. As a consequence, this system does not show any gas–liquid critical points.

Our results yield a picture of a system that exhibits interesting thermodynamic properties and phase behavior and contribute to a better understanding of the mechanism underlying the spontaneous formation of self-assembled structures in a large variety of systems, such as biological macromolecules, peptide amphiphiles, and surfactants.

APPENDIX

Free-Energy Calculations

Methods to calculate the free energy for fluids and crystals are well-established. For completeness we give more details in the following. We write the free energy per particle and the energy per particle as $f = F/N$ and $u = U/N$, respectively, where F is the free energy and U is the energy.

Fluid. The absolute free energies of the fluid are calculated using thermodynamic integration over β at constant density and adding a hard sphere contribution to the free energy. The hard sphere contribution is evaluated using the Carnahan–Starling equation

$$\beta f_{\text{HS}} = \ln(\rho\Lambda^3) - 1 + \frac{4\eta - 3\eta^3}{(1 - \eta)^2} \quad (8)$$

where Λ^3 is the thermal volume of a single particle and η is the packing fraction; $\rho = N/V$ is the number density. The equation to obtain the fluid free energy is

$$\beta f = \beta f_{\text{HS}} + \int_0^\beta \langle u \rangle_{N,V,\beta'} d\beta' \quad (9)$$

Multiple constant *NVT* MC simulations were performed at number density $\rho\sigma^3 = 0.3$ to evaluate this integral.

Crystals. The absolute crystal free energies are calculated using the Frenkel–Ladd method, where the reference Hamiltonian is split into two parts. One part contains translational degrees of freedom ($\mathcal{H}_{\text{ref}}^{\text{trans}}$), and the other part contains orientational degrees of freedom ($\mathcal{H}_{\text{ref}}^{\text{or}}$). The translational reference Hamiltonian corresponds to an Einstein crystal with a fixed center of mass, and it reads

$$\mathcal{H}_{\text{ref}}^{\text{trans}}(\lambda^{\text{trans}}) = \lambda^{\text{trans}} \sum_{i=1}^N |\mathbf{r}_i - \mathbf{r}_{i,0} - \mathbf{r}_{\text{cm}}|^2 \quad (10)$$

where λ is a coupling parameter, \mathbf{r}_i the position of particle i , $\mathbf{r}_{i,0}$ its reference position, and \mathbf{r}_{cm} the center of mass of the crystal. In principle, the orientational reference Hamiltonian can be chosen arbitrarily.⁵⁵ It is, however, far more convenient to choose a Hamiltonian that reflects the symmetry of the calculated system. In our case, we use the ($C_{\infty v}$ -symmetric) reference orientational already mentioned in ref 35, with a Hamiltonian that reads

$$\mathcal{H}_{\text{ref}}^{\text{or}}(\lambda^{\text{or}}) = \lambda^{\text{or}} \sum_{i=1}^N [1 - \cos(\phi)] \quad (11)$$

where ϕ is the angle between the orientation of the particle and the orientation inside the reference crystal. In this work, we set $\lambda = \lambda^{\text{trans}} = \lambda^{\text{or}}$.

During the free-energy calculation, the particle interactions are described with a combined Hamiltonian

$$\mathcal{H}' = \mathcal{H} + \mathcal{H}_{\text{ref}} \quad (12)$$

where \mathcal{H} is the Kern–Frenkel Hamiltonian

$$\mathcal{H} = \sum_{i=1}^N \sum_{j=i+1}^{N-1} u^{\text{KF}}(\mathbf{r}_{ij}, \hat{\mathbf{n}}_i, \hat{\mathbf{n}}_j) \quad (13)$$

The reference Hamiltonian is

$$\mathcal{H}_{\text{ref}} = \mathcal{H}_{\text{ref}}^{\text{trans}} + \mathcal{H}_{\text{ref}}^{\text{or}} \quad (14)$$

The free-energy difference between the reference system and the investigated system is

$$\Delta f = f(0)_{N,V,T} - f(\lambda_{\text{max}})_{N,V,T} \quad (15)$$

$$= \int_0^{\lambda_{\text{max}}} \left\langle \frac{d\mathcal{H}_{\text{ref}}(\lambda)}{d\lambda} \right\rangle_{N,V,T,\lambda} d\lambda \quad (16)$$

The integral is evaluated using series of constant *NVT* simulations with the combined Hamiltonian. To properly evaluate the integral, λ_{max} has to be made sufficiently large such that the particle positions and orientations are coupled to those of the reference crystal and the free energy of the real system converges to that of the reference system. The reference free energy at λ_{max} is

$$\beta f_{\text{ref}}(\lambda_{\text{max}}) = \beta f_{\text{ref}}^{\text{trans}}(\lambda_{\text{max}}) + \beta f_{\text{ref}}^{\text{or}}(\lambda_{\text{max}}) \quad (17)$$

where the translational free energy of the reference system reads

$$\begin{aligned} \beta f_{\text{ref}}^{\text{trans}}(\lambda_{\text{max}}) &= \beta f_{\text{Ein}}^{\text{trans}}(\lambda_{\text{max}}) \\ &= -\frac{1}{N} \ln \left[\left(\frac{1}{\Lambda_t} \right)^{3N} \left(\frac{\pi}{\beta \lambda_{\text{max}}} \right)^{3(N-1)/2} N^{1/2V} \right] \end{aligned} \quad (18)$$

where $\Lambda_t = h/(2\pi m k_B T)^{1/2}$; h is Planck's constant and m is the mass of a particle. The orientational free energy of the reference system reads

$$\beta f_{\text{ref}}^{\text{or}}(\lambda_{\text{max}}) = -\ln \frac{1}{\Lambda_r} \frac{1 - \exp(-2\beta \lambda_{\text{max}})}{2\beta \lambda_{\text{max}}} \quad (19)$$

where $\Lambda_r = h^2/(8\pi^2 I k_B T)$ and I is the moment of inertia of the particle. The values of Λ and Λ_r have no effect on the equilibrium phase behavior; thus, we can safely state $\Lambda = \Lambda_r \Lambda_t = \sigma^3$. The free energy of the real system is the sum

$$\beta f = \beta \Delta f(\lambda_{\text{max}}) + \beta f_{\text{ref}}(\lambda_{\text{max}}) + \beta u_{\text{en}} \quad (20)$$

where u_{en} is the energy per particle in the reference crystal.

A 41-point Gauss–Legendre quadrature is used to evaluate the integral in eq 16. In our free-energy calculations we chose a value of $\lambda_{\text{max}} = 10^7 \epsilon$.

AUTHOR INFORMATION

Corresponding Author

*E-mail: teun.vissers@roma1.infn.it.

Notes

The authors declare no competing financial interest.

ACKNOWLEDGMENTS

We acknowledge support from ERC-226207-PATCHYCOLLOIDS, ITN-234810-COMPLOIDS, and MIUR-PRIN.

REFERENCES

- (1) van Jaarsveld, J.; van der Schoot, P. Scaling Theory of Interacting Thermally Activated Supramolecular Polymers. *Macromolecules* **2007**, *40*, 2177.
- (2) Smulders, M. M. J.; Nieuwenhuizen, M. M. L.; de Greef, T. F. A.; van der Schoot, A. P. H. J.; Schenning, P.; Meijer, E. W. How to Distinguish Isodesmic from Cooperative Supramolecular Polymerisation. *Chem.—Eur. J.* **2010**, *16*, 362.
- (3) Smulders, M. M. J.; Pilot, I. A. W.; Leenders, J. M. A.; van der Schoot, P.; Palmans, A. R. A.; Schenning, A. P. H. J.; Meijer, E. W. Tuning the Extent of Chiral Amplification by Temperature in a Dynamic Supramolecular Polymer. *J. Am. Chem. Soc.* **2010**, *132*, 611.
- (4) Chen, Q.; Bae, S. C.; Granick, S. Directed Self-Assembly of a Colloidal Kagome Lattice. *Nature* **2011**, *469*, 381–384.
- (5) Glotzer, S. C.; Solomon, M. J. Anisotropy of Building Blocks and Their Assembly into Complex Structures. *Nat. Mater.* **2007**, *6*, 557–562.
- (6) Sacanna, S.; Pine, D. J. Shape-Anisotropic Colloids: Building Blocks for Complex assemblies. *Curr. Opin. Colloid Interface Sci.* **2011**, *16*, 96.
- (7) Wang, Y.; Wang, Y.; Breed, D. R.; Manoharan, V.; Feng, L.; Hollingsworth, A. D.; Weck, M.; Pine, D. J. Colloids with Valence and Specific Directional Bonding. *Nature* **2012**, *491*, 51.
- (8) Manoharan, V. N.; Elsesser, M. T.; Pine, D. J. Dense Packing and Symmetry in Small Clusters of Microspheres. *Science* **2003**, *301*, 483–487.

(9) Pawar, A. B.; Kretzschmar, I. Fabrication, Assembly, and Application of Patchy Particles. *Macromol. Rapid Commun.* **2010**, *31*, 150–168.

(10) Zhang, Z.; Glotzer, S. C. Self-Assembly of Patchy Particles. *Nano Lett.* **2004**, *4*, 1407–1413.

(11) Chen, Q.; Whitmer, J. K.; Jiang, S.; Bae, S. C.; Luijten, E.; Granick, S. Supramolecular Reaction Kinetics of Janus Spheres. *Science* **2011**, *331*, 199.

(12) Chen, Q.; Yan, J.; Zhang, J.; Bae, S. C.; Granick, S. Janus and Multiblock Colloidal Particles. *Langmuir* **2012**, *28*, 13555.

(13) Mao, X.; Chen, Q.; Granick, S. Entropy Favours Open Colloidal Lattices. *Nat. Mater.* **2013**, *12*, 217.

(14) Kraft, D. J.; Groenewold, J.; Kegel, W. K. Colloidal Molecules with Well-Controlled Bond Angles. *Soft Matter* **2009**, *5*, 3823–3826.

(15) Kraft, D. J.; Hilhorst, J.; Heinen, M. A. P.; Hoogenraad, M. J.; Luigjes, B.; Kegel, W. K. Patchy Polymer Colloids with Tunable Anisotropy Dimensions. *J. Phys. Chem. B* **2011**, *115*, 7175.

(16) Giacometti, A. Self-Assembly Mechanism in Colloids: Perspectives from Statistical Physics. *Cent. Eur. J. Phys.* **2012**, *10*, 540–551.

(17) Gögelein, C.; Romano, F.; Sciortino, F.; Giacometti, A. Fluid-Fluid and Fluid-Solid Transitions in The Kern-Frenkel Model from Barker-Henderson Thermodynamic Perturbation Theory. *J. Chem. Phys.* **2012**, *136*, 094512.

(18) Giacometti, A.; Lado, F.; Largo, J.; Pastore, G.; Sciortino, F. Phase Diagram and Structural Properties of a Simple Model For One-Patch Particles. *J. Chem. Phys.* **2009**, *131*, 174114.

(19) Giacometti, A.; Lado, F.; Largo, J.; Pastore, G.; Sciortino, F. Effects of Patch Size and Number within a Simple Model of Patchy Colloids. *J. Chem. Phys.* **2010**, *132*, 174110.

(20) Tavares, J.; Teixeira, P.; Telo da Gama, M. How Patchy Can One Get and Still Condense? The Role of Dissimilar Patches in The Interactions of Colloidal Particles. *Mol. Phys.* **2009**, *107*, 453–466.

(21) Tavares, J. M.; Teixeira, P. I. C.; Telo da Gama, M. M. Criticality of Colloids with Distinct Interaction Patches: The Limits of Linear Chains, Hyperbranched Polymers, and Dimers. *Phys. Rev. E: Stat., Nonlinear, Soft Matter Phys.* **2009**, *80*, 021506.

(22) Tavares, J. M.; Teixeira, P. I. C.; Telo da Gama, M. M.; Sciortino, F. Equilibrium Self-Assembly of Colloids with Distinct Interaction Sites: Thermodynamics, Percolation, and Cluster Distribution Functions. *J. Chem. Phys.* **2010**, *132*, 234502.

(23) Bianchi, E.; Blaak, R.; Likos, C. Patchy Colloids: State of the Art and Perspectives. *Phys. Chem. Chem. Phys.* **2011**, *13*, 6297.

(24) Roh, K.-H.; Martin, D. C.; Lahann, J. Biphasic Janus Particles with Nanoscale Anisotropy. *Nat. Mater.* **2005**, *4*, 759–763.

(25) Wang, B.; Li, B.; Zhao, B.; Li, C. Y. Amphiphilic Janus Gold Nanoparticles via Combining “Solid-State Grafting-to” and “Grafting-from” Methods. *J. Am. Chem. Soc.* **2008**, *130*, 11594–11595.

(26) Chen, C.-H.; Shah, R. K.; Abate, A. R.; Weitz, D. A. Janus Particles Templated from Double Emulsion Droplets Generated Using Microfluidics. *Langmuir* **2009**, *25*, 4320–4323.

(27) Jackson, A. M.; Myerson, J. W.; Stellacci, F. Spontaneous Assembly of Subnanometre-Ordered Domains in the Ligand Shell of Monolayer-Protected Nanoparticles. *Nat. Mater.* **2004**, *3*, 330–336.

(28) Jiang, B. S.; Chen, Q.; Tripathy, M.; Luijten, E.; Schweizer, K.; Granick, S. Janus Particle Synthesis and Assembly. *Adv. Mater. (Weinheim, Ger.)* **2010**, *22*, 1060.

(29) Hong, L.; Cacciuto, A.; Luijten, E.; Granick, S. Clusters of Charged Janus Spheres. *Nano Lett.* **2006**, *6*, 2510–2514.

(30) Walther, A.; Müller, H. Janus Particles. *Soft Matter* **2008**, *4*, 663.

(31) Munaò, G.; Preisler, Z.; Vissers, T.; Smallenburg, F.; Sciortino, F. Cluster Formation in One-Patch Colloids: Low Coverage Results. *Soft Matter* **2013**, *9*, 2652–2661.

(32) Kern, N.; Frenkel, D. Fluid-Fluid Coexistence in Colloidal Systems with Short-Ranged Strongly Directional Attraction. *J. Chem. Phys.* **2003**, *118*, 9882–9889.

(33) Sciortino, F.; Giacometti, A.; Pastore, G. A Numerical Study of One-patch Colloidal Particles: From Square-Well to Janus. *Phys. Chem. Chem. Phys.* **2010**, *12*, 11869–11877.

- (34) Sciortino, F.; Giacometti, A.; Pastore, G. Phase Diagram of Janus Particles. *Phys. Rev. Lett.* **2009**, *103*, 237801.
- (35) Vissers, T.; Preisler, Z.; Smalenburg, F.; Dijkstra, M.; Sciortino, F. Predicting Crystals of Janus Colloids. *J. Chem. Phys.* **2013**, *138*, 164505.
- (36) Lara, C.; Usov, I.; Adamcik, J.; Mezzenga, R. Sub-Persistence-Length Complex Scaling Behavior in Lysozyme Amyloid Fibrils. *Phys. Rev. Lett.* **2011**, *107*, 238101.
- (37) Lara, C.; Adamcik, J.; Jordens, S.; Mezzenga, R. General Self-Assembly Mechanism Converting Hydrolyzed Globular Proteins Into Giant Multistranded Amyloid Ribbons. *Biomacromolecules* **2011**, *12*, 1868.
- (38) Raccosta, S.; Martorana, V.; Manno, M. Thermodynamic versus Conformational Metastability in Fibril-Forming Lysozyme Solutions. *J. Phys. Chem. B* **2012**, *116*, 12078–12087.
- (39) Won, Y.-Y.; Davis, H. T.; Bates, F. S. Giant Wormlike Rubber Micelles. *Science* **1999**, *283*, 960–963.
- (40) Yang, J. Viscoelastic Wormlike Micelles and Their Applications. *Curr. Opin. Colloid Interface Sci.* **2002**, *7*, 276–281.
- (41) Meng, Q.; Kou, Y.; Ma, X.; Liang, Y.; Guo, L.; Ni, C.; Liu, K. Tunable Self-Assembled Peptide Amphiphile Nanostructures. *Langmuir* **2012**, *28*, 5017.
- (42) Diful, A. G.; Avalos, J. B.; Mackie, A. D. Model Shape Transitions of Micelles: Spheres to Cylinders and Disks. *Langmuir* **2012**, *28*, 3730.
- (43) Li, Z.-W.; Lu, Z.-Y.; Sun, Z.-Y.; An, L.-J. Model, Self-Assembly Structures, and Phase Diagram of Soft Janus Particles. *Soft Matter* **2012**, *8*, 6693–6697.
- (44) Filion, L.; Marechal, M.; van Oorschot, B.; Pelt, D.; Smalenburg, F.; Dijkstra, M. Efficient Method for Predicting Crystal Structures at Finite Temperature: Variable Box Shape Simulations. *Phys. Rev. Lett.* **2009**, *103*, 188302.
- (45) Chen, B.; Siepman, J. I. A Novel Monte Carlo Algorithm for Simulating Strongly Associating Fluids: Applications to Water, Hydrogen Fluoride, and Acetic Acid. *J. Phys. Chem. B* **2000**, *104*, 8725–8734.
- (46) Chen, B.; Siepman, J. I. Improving the Efficiency of the Aggregation–Volume–Bias Monte Carlo Algorithm. *J. Phys. Chem. B* **2001**, *105*, 11275–11282.
- (47) Kofke, D. A. Direct Evaluation of Phase Coexistence by Molecular Simulation via Integration along the Saturation Line. *J. Chem. Phys.* **1993**, *98*, 4149–4162.
- (48) Romano, F.; Sanz, E.; Tartaglia, P.; Sciortino, F. Phase Diagram of Trivalent and Pentavalent Patchy Particles. *J. Phys.: Condens. Matter* **2012**, *24*, 064113.
- (49) Romano, F.; Sanz, E.; Sciortino, F. Phase Diagram of a Tetrahedral Patchy Particle Model for Different Interaction Ranges. *J. Chem. Phys.* **2010**, *132*, 184501.
- (50) Bianchi, E.; Doppelbauer, G.; Filion, L.; Dijkstra, M.; Kahl, G. Predicting Patchy Particle Crystals: Variable Box Shape Simulations and Evolutionary Algorithms. *J. Chem. Phys.* **2012**, *136*, 214102.
- (51) de Graaf, J.; Filion, L.; Marechal, M.; van Roij, R.; Dijkstra, M. Crystal-Structure Prediction via the Floppy-Box Monte Carlo Algorithm: Method and Application to Hard (Non)Convex Particles. *J. Chem. Phys.* **2012**, *137*, 214101.
- (52) Fantoni, R.; Giacometti, A.; Sciortino, F.; Pastore, G. Cluster Theory of Janus Particles. *Soft Matter* **2011**, *7*, 2419–2427.
- (53) Kraft, D. J.; Ni, R.; Smalenburg, F.; Hermes, M.; Yoon, K.; Weitz, D. A.; van Blaaderen, A.; Groenewold, J.; Dijkstra, M.; Kegel, W. K. Surface Roughness Directed Self-Assembly of Patchy Particles into Colloidal Micelles. *Proc. Natl. Acad. Sci. U.S.A.* **2012**, *109*, 10787–10792.
- (54) Coniglio, A.; Klein, W. Clusters and Ising Critical Droplets: A Renormalization Group Approach. *J. Phys. A* **1980**, *13*, 2775.
- (55) Noya, E. G.; Vega, C.; Doye, J. P.; Louis, A. A. The Stability of a Crystal with Diamond Structure for Patchy Particles with Tetrahedral Symmetry. *J. Chem. Phys.* **2010**, *132*, 234511.